Optimizing Gradient Structural Resonance Compliant Acoustic Liner for Duct-Flow Noise Mitigation

A. Abdullah, and Adrian W.K. Lam,
Randolph C.K. Leung*

Department of Mechanical Engineering, The Hong Kong Polytechnic University, Kowloon, Hong Kong, P. R. China.

This study attempts to optimize the broadband low-frequency noise reduction using compliant acoustic liners in flow ducts. The analytical model for a single compliant unit is extended to multiple fluid-loaded compliant units acoustic liner mounted along a rigid duct wall in uniform duct flow. Each compliant unit is a tensioned elastic panel backed by a rigid cavity, and its fluid-loaded structural resonance is obtained by coupling the structural impedance of the panel with the acoustic impedance of the backing cavity. In the study, cavity depth and in-plane panel tension are treated as independent design variables that govern the location and bandwidth of transmission stopbands. A genetic algorithm is then employed to optimize the design variables over prescribed intervals, to maximize transmission loss over a target low-frequency band under geometric and structural constraints. The optimized liner designs show performance improvement in the location and width of the stopband. Moreover, it also confirms that optimized distributions of cavity depth and panel tension can merge multiple narrow resonant peaks into a broad low-frequency region of elevated transmission loss. The transmission loss (*TL)* stopband, is effectively broadened from $0.043 \leq f \leq 0.07$ in uniform resonance distribution configuration to $0.02 \leq f \leq 0.07$ in the optimized design, thus providing an overall 85.0% increase in stopband bandwidth. The performance of the optimized design compliant liner is subsequently studied using a high-fidelity time-domain perturbation evolution method for exploring the underlying aeroacoustic structural interaction.

Keywords: Optimization, Genetic Algorithm, Transmission loss, Low-frequency regime, Perturbation evolution method

---

*Corresponding author: (mmrleung@polyu.edu.hk). Senior member AIAA.

1. Introduction

Flow duct systems, such as ventilation and air-conditioning duct networks, exhaust ducts, often transmit significant low-frequency noise to surrounding environments [1–3]. Generally, passive liners, based on bulk porous materials or cavity-backed perforated faces, reduce sound by viscous dissipation and periodic flow through small pores, but they are most effective where particle velocity is high and therefore demand a quarter-wavelength cavity depth for good performance. However, for the low-frequency regime, this constraint leads to bulky designs that are difficult to integrate, while the rough surfaces of fibrous absorbers introduce aerodynamic losses and may be incompatible with applications such as aero-engines, where hydrocarbon contamination is a concern. Micro-perforated panel (MPP) liners and slow-sound concepts have been proposed to alleviate some of these drawbacks and to push effective absorption to lower frequencies, but their performance still degrades in the presence of grazing flow, and their stopband bands are governed by fixed geometrical resonances [4,5]. In parallel with these passive acoustic liners, there has been a sustained effort to characterize and model the propagation of sound in lined ducts with reacting liners in the presence of mean flow [6–8]. Mode-matching and numerical eigenmode analyses have shown that uniform mean flow modifies axial wavenumbers and mode shapes in lined rectangular or annular ducts, and that the validity of the locally reacting approximation deteriorates for long or shallow cavities or for strongly dispersive liner materials [9,10]. Numerous studies have examined the aeroacoustic behaviour of micro-perforated, resonant, and metamaterial-type liners under grazing flows. Experiments on perforated pipes with grazing flow have revealed strong sensitivity of absorption to both flow components and to porosity, with distinct optimal open-area ratios emerging at low Mach and Strouhal numbers [11]. The numerical and experimental studies of Helmholtz-type or multi-cavity resonators have shown that geometry and flow conditions control resonance frequency, and that coupled resonators can broaden the

effective stopband but are susceptible to flow-induced detuning [12]. Zhang and Cheng [13] showed that grazing flow tends to shift TL peaks to higher frequencies, reduce peaks TL, and broaden the effective bandwidth, and that cavity partitioning, perforation parameters, and panel length jointly control the balance between reflection-dominated and absorption-dominated noise mitigation [13]. These studies emphasize that both locally resonant and flow-aware impedance modelling are critical for achieving robust broadband low-frequency noise mitigation performance.

Motivated by aforementioned limitations, a tensioned elastic panel flush-mounted in a rigid duct as a vibrating wall can provide low-frequency noise mitigation by combining reflective and dissipative mechanisms [14–17]. In this concept, an incident plane wave excites flexural waves in the panel; energy is dissipated via structural damping, and a sudden change of wall compliance interacts with the acoustic waves above the liner, creating impedance mismatch, strong reflection, and stop/pass bands across the frequency range. Subsequent theoretical and experimental studies extended the analysis to cavity-backed configurations in which the panel is covered on its exterior side to prevent noise breakout, so that the panel and backing cavity form a coupled vibroacoustic system; the cavity then modifies panel dispersion, shifts fluid-loaded resonance frequencies, and introduces additional cavity modes that interact with the panel motion. It has been established that analytical models based on modal expansions and scattering models provide the net transmitted field by superposition of the incident wave and the scattered field generated by the panel [14–17].

In recent studies, the detailed time-domain numerical studies of cavity-backed elastic panel (EP) liners under grazing flow were conducted. Fan et al.[18] employed a direct aeroacoustic simulation (DAS) framework based on the two-dimensional compressible Navier–Stokes equations solved by the Conservation Element and Solution Element (CESE) method, which was validated against the benchmark experiments of Choy and Huang et al.

[17]. Their broadband analysis showed that the elastic panel liner exhibits several low-transmission bands in which reflection dominates at low frequencies and absorption gradually becomes more important at higher frequencies; the scattered wave generated by the panel was found to be a superposition of subsonic and supersonic flexural components whose phase relation with the incident wave controls the *TL*. When a subsonic boundary-layer flow is introduced, they observed that flow opposing the incident wave strongly enhances absorption and can even create additional low-transmission bands at higher frequencies, whereas flow aligned with the excitation mainly weakens reflection and narrows existing bands, with the overall liner performance remaining markedly better when the noise source radiates against the flow. Moreover, Lam et al. [19] performed a comprehensive parametric study of the effect of backing-cavity configuration on the performance of cavity-backed EP liners under low-Mach grazing. In this study, cavity depth, panel length, and cavity shape, and by introducing absorptive material inside the cavity, they showed that the backing cavity plays an important role in both reflective and absorptive mechanisms. For relatively deep rectangular cavities, multiple low-transmission bands arise in which *TL* peaks can exceed 30 dB; reflection dominates in the lower bands, and absorption peaks coincide with strong resonant panel vibration and higher-order cavity modes. As the cavity becomes very shallow, the air in the cavity behaves as a stiff spring, raising the critical frequency of the supersonic flexural branch and severely weakening panel response except at resonance; in this regime, *TL* peaks are closely aligned with resonant panel modes, and the noise mitigation mechanism is dominated by resonant radiation and fluid-loading losses rather than broadband interference. Non-rectangular cavities, formed by varying the base length while keeping the opening fixed, were found to generate non-planar cavity modes and to decorrelate panel and cavity responses, leading to frequency-dependent enhancements or degradations in *TL* relative to the rectangular case but no uniformly superior configuration. Finally, by placing a highly absorptive treatment

at the downstream side of the cavity, Lam et al. [19] demonstrated that it is possible to relieve cavity acoustics, suppress radiation back into the duct, and significantly enhance broadband absorption while simultaneously reducing reflected levels, a promising concept for practical liners where strong backward radiation is undesirable.

Furthermore, Abdullah et al. [20] investigated the mitigation of broadband duct-flow noise using a liner with gradient surface resonant compliance, in which multiple cavity-backed elastic panel units are flush-mounted along the duct walls, and their fluid-loaded resonant frequencies are deliberately varied to create overlapping low-frequency stopbands. Using a reduced-order perturbation evolution method (PEM) embedded in a CESE-based direct aeroacoustic simulation framework, the study compared uniform, increasing, and decreasing resonance distributions along the streamwise direction, demonstrating that gradient designs can broaden the low-frequency stopband and increase overall transmission loss while keeping the drag penalty significantly below that of conventional acoustic liners. In practical systems, duct-length constraints and the need for robust broadband performance naturally favour multi-unit liners in which several panel–cavity cells with distinct resonance surface compliance are distributed along the flow direction, by spatially varying compliance properties.

The present study aims to address this gap by formulating a genetic parametric optimization framework that exploits the design insights from our earlier studies of multi-unit liner. In the first stage, the modal expansion-based analytical model for a single cavity-backed elastic panel is extended to a five-unit compliant liner analytical model using transfer matrix method, each unit characterised by its panel tension and cavity depth, and embedded in a low-Mach grazing flow, so that the influence of multi-unit resonance distributions on low-frequency *TL* can be systematically examined. A genetic algorithm is employed to more effectively search the panel-cavity parameter space under constraints on manufacturability, duct integration, and prescribed monotonic gradient trends along the flow direction [21]. The

baseline case with uniform resonance distribution (URD) serves as a reference. Unconstrained genetic runs explore the best achievable broadband performance without any constraint of monotonic gradient. Gradient-constrained optimization enforces either a linearly increasing or decreasing gradient, depending on *TL* performance. The analytically predicted *TL* spectra of selected designs are then re-evaluated in the presence of grazing flow, and a subset of optimal configurations is further validated using fully coupled CESE-PEM. By comparing the optimised multi-unit compliant liners against the *TL* performance of compliant liner from previous studies, we show that appropriately graded distributions of fluid-loaded panel resonances can deliver competitive or superior broadband low-frequency *TL* in ducts with grazing flow, while retaining the advantages of low flow-induced pressure loss and structural simplicity that motivated the original elastic-panel concept.

2. Methodology

This study combines an analytical model for a multi-unit compliant liner with a genetic algorithm (GA) for parametric optimization, followed by high-fidelity numerical study using a time-domain CESE–PEM solver monolithically coupled with the panel structural dynamics. The overall methodology consists of three steps: (i) extend the formulation of a single-unit analytical model to a multi-unit liner; (ii) use this analytical model as a solver inside a GA to optimize panel tension and cavity depth distributions; and (iii) validate the selected optimized designs with the high-fidelity numerical study using CESE framework [20].

2.1. Analytical model for a single cavity-backed elastic panel unit

The analytical model for a single compliant unit shown in Fig. 2.1 follows the membrane–cavity formulation of modal analysis of a drum-like silencer [15]. The configuration consists of a two-dimensional rigid duct of height h^*, partially lined on the lower wall by a tensioned elastic panel of length L_p^*, backed by a rigid rectangular cavity of depth D_c^*. The elastic panel is simply supported at $x_p^* = \pm\frac{L_p^*}{2}$, and is excited by a unit-amplitude plane wave grazing along the duct, $p_i^* = \exp\big(i(\omega^* t^* - k_0^* x^*)\big)$, where $\omega^* = 2\pi f^*$ and $k_0^* = \frac{\omega^*}{c_0^*}$. In order to include the uniform flow effects in the analytical model, a convective term is included in the equation wave number by using Mach number (M_∞), thus giving an effective wave number ($k_{eff} = \frac{k_0^*}{1\pm M_\infty}$) [22]. All variables are normalized using ambient air density ρ_0^*, half-duct width $h^*/2$, ambient acoustic speed c_0^*, and pressure by $\rho_0^* c_0^{*2}$, where the quantities with asterisk ($*$) are dimensional variables.

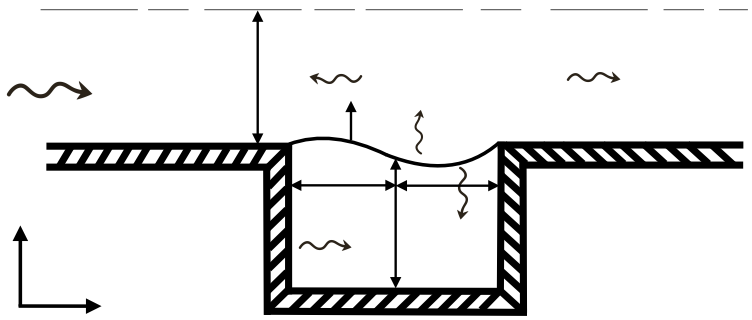

Single panel-cavity configuration for analytical model

In the duct regions upstream and downstream of the membrane section, only a plane-wave is considered, so the total pressure is written as a superposition of incident, reflected, and transmitted waves plus the scattered field radiated by the membrane. Inside the backing cavity, the acoustic pressure on the cavity side of the membrane is expanded in the normal modes of the rigid-walled cavity. The elastic panel is treated as a thin, non-porous, tensioned panel, and its dynamics w_p is solved using the one dimensional plate equation.

$$D\frac{\partial^4 w_p}{\partial x^4} - \frac{T_p \partial^2 w_p}{\partial x^2} + \frac{\rho_p h_p \partial^2 w_p}{\partial t^2} + \frac{C_p(\partial w_p)}{\partial t} = p_+ - p_- \tag{1}$$

Its transverse displacement $w_p(x,t)$ is expanded in simply supported *in-vacuo* modes,

$$w_p(x,t) = \sum_{n=1}^{\infty} w_n(t)\,\phi_n(x)$$

where $\phi_n(x) = \sin\left(n\pi\left(\frac{x + L_p/2}{L}\right)\right)$, and the modal amplitudes w_n satisfy coupled ordinary differential equations obtained by projecting the panel equation of motion onto ϕ_n. Introducing harmonic fluctuations, the panel vibration velocity $V = i\omega w_p$ in Eq. 1 becomes;

$$\frac{D}{i\omega}\frac{\partial^4 V}{\partial x^4} - \frac{T_p}{i\omega}\frac{\partial^2 V}{\partial x^2} + \rho_p h_p i\omega V + C_p V = (p_+ - p_-) \tag{2}$$

The standard Galerkin procedure is applied to solve Eq. 2. Therefore, the transverse velocity V for the elastic panel simply supported at the two ends can be expanded as a series of in *vacuo* modes with modal amplitude V_j using a dimensionless variable $\xi = \frac{x_p}{L_p} + \frac{1}{2}$.

$$V = \sum_{j=1}^{\infty} V_j \sin j\pi\xi \qquad \text{where} \qquad V_j = 2\int_0^1 V_{(\xi,t)} \sin(j\pi\xi)\, d\xi.$$

Substituting V in to Eq. 2 leads to a system of linear equations as below;

$$\mathcal{L}V_j + 2\int_0^1 (p_+ - p_-)\, \sin(j\pi\xi) d\xi\,, \tag{3}$$

where $\mathcal{L}$ is defined as the structural impedance of the elastic panel,

$$\mathcal{L} = \frac{D}{i\omega}\left(\frac{j\pi}{L}\right)^4 + \frac{T}{i\omega}\left(\frac{j\pi}{L}\right)^2 + \rho_p h_p i\omega + C_p.$$

The fluid–structure coupling is due to the fluid-loading $(p_+ - p_-)$ resulting from the net pressure difference across the panel. The $(p_+ - p_-)$ consists of the pressure radiation from the elastic panel into the duct side, i.e. p_{+rad} , and pressure radiation into the cavity p_{-rad}, while p_{-ref} is the pressure fluctuation due to reflection in the cavity.

$$(p_+ - p_-) = p_i + p_{+rad} + p_{-rad} + p_{-ref}$$

The pressure radiation p_{+rad} in the duct can be estimated using the Doak's expression [23].

$$p_{+rad}(x,y) = \frac{L_p}{2}\sum_{r=0}^{\infty} c_r \psi_r(y) \int_0^1 \begin{matrix}[H(x - x')e^{-ik_0(x-x')} + \\ H(x'-x)(e^{-ik_0(x-x')}]\psi_r(y)V(x')d\xi\end{matrix}$$

Hence, the modal impedance Z_{jl} due to panel radiation in the duct can be estimated as follows.

$$Z_{jl} = L_p \sum_{r=0}^{\infty} c_r(2 - \delta_{0r})\, I_2(r,j,l) \tag{4}$$

Similarly, the cavity side radiation pressure (p_{-rad}) is also given below,

$$p_{-rad}(x, x_c) = \frac{L_c}{2}\sum_{r=0}^{\infty} c_{rc}\psi_r(y_c)\int_0^1 \psi_r(y_c')[-V(x_c')] * [H(x_c - x_c')e^{-ik_{rc}(x_c - x_{c'})} + H(x_c' - x_c)(e^{ik_{rc}(x_c - x_{c'})}]d\xi \quad (5)$$

The modal impedance in the cavity Z_{-jl} due to panel radiation p_{-rad} is estimated as follows,

$$Z_{-jl} = L_c \sum_{r=0}^{\infty} c_{rc}(2 - \delta_{0r})\, I_{2c}(r, j, l)$$

where I_2 and I_{2c} is the double integration. Similarly, the acoustic reflection in the cavity can be estimated by

$$dp_{-ref} = \frac{L_c}{2}\sum_{r=0}^{\infty} c_{rc}\psi_r(y_c)\,\psi_r(y_c') * [Ae^{-ik_{rc}(x_c - x_{c'})}B(e^{ik_{rc}(x_c - x_{c'})}][-V(x_c')]d\xi' \quad (6)$$

where, coefficients *A* and *B* are found by rigid wall boundary condition.

$$\left.\frac{\partial(p_{-rad} + p_{-ref})}{\partial x_c}\right|_{|x_c| = L_c/2} = 0$$

Substituting in Eq. 6 we get

$$p_{-ref} = \frac{L_c}{2}\sum_{r=0}^{\infty} c_{rc}\psi_r(y_c)\int_0^1 \psi_n(y_c')[-V(x_c')] * \frac{2}{e^{ik_{rc}(2L_c)}}\left[\cos k_{rc}(x_c - x_c') + e^{ik_{rc}L_c}\cos k_{rc}(x_c + x_c')\right]d\xi \quad (7)$$

Hence, we can now find the modal reflection Z_{rjl}.

$$Z_{rjl} = L_c \sum_{r=0}^{\infty} c_{nc}(2 - \delta_{0r})\, I_{2r}(r, j, l)$$

The expressions for I , I I_{2r} and the details of the above formulation can be found in the study [14–16]. The total modal impedance $Z_t = Z_{jl} + Z_{-jl} + Z_{rjl}$ includes the structural tension, membrane mass, and pressure radiation due to fluid-loading and cavity reflection. Therefore,

once the modal impedance of cavity and duct regions along with the structural impedance of the elastic panel are determined, we may find the modal vibration amplitudes V_j as follows

$$V = -Z_t^{-1} I$$

$$V = \begin{bmatrix} V_1 \\ V_2 \\ \vdots \\ \vdots \\ V_n \end{bmatrix}, Z_t = \begin{bmatrix} Z_{11} + \mathcal{L}_{11} & \cdots & Z_{1N} \\ \vdots & \ddots & \vdots \\ Z_{N1} & \cdots & Z_{NN} + \mathcal{L}_{NN} \end{bmatrix}, I = \begin{bmatrix} I \\ I_2 \\ \vdots \\ \vdots \\ I_n \end{bmatrix}$$

where, I is the modal incident excitation matrix given as

$$I = 2\int_0^1 p_i \sin(j\pi\xi)\, d\xi$$

Therefore, with anechoic downstream termination, the complex pressure reflection and transmission coefficients $\frac{p_{ref}}{p_i} = \mathcal{R}$, $\frac{p_{rad}}{p_i} = \mathcal{T}$ respectively, at the upstream and downstream junctions of the compliant unit are obtained using the vibrational amplitudes V_j as detailed in Ref. [15]. The transmission loss along the duct with an incident wave of unit amplitude, $|p_i| = 1$, is defined as TL = -20*$log_{10}|\, p_t/p_i|$ where $p_t = p_{rad} + p_i$.

2.2. Extending single unit analytical to multi-unit Liner

In this section, the single-unit analytical model shown in Fig. 2.1 is used as the building block for the multi-unit analytical model. We compute the modal impedances, solve the coupled system, and tabulate the resulting single-unit *TL*. These unit-cell responses are then used by the transfer matrix method to predict the multi-unit liner response as shown by Choy et al. [24], and the subsequent parametric genetic optimization of the gradient surface resonant compliance is also performed. The acoustic coefficients p_r and p_t from each compliant unit solved above in Section 2.1 are used to construct the respective transfer matrix $\boldsymbol{M}$. This transfer matrix relates the state variable S at the upstream (S_{up}) location to the downstream (S_{dn}) location of each compliant unit as below

$$S_{up} = MS_{dn}$$

where, $\boldsymbol{M} = \begin{bmatrix} M_{11} & M_{12} \\ M_{21} & M_{22} \end{bmatrix}$

Therefore, we relate the incident, reflected, and transmitted acoustic coefficients as below

$$\begin{bmatrix} p_i + p_r \\ p_i - p_r \end{bmatrix} = \boldsymbol{M} \begin{bmatrix} p_t \\ p_t \end{bmatrix} \tag{8}$$

$$\begin{bmatrix} p_t \\ p_t \end{bmatrix} = \boldsymbol{M} \begin{bmatrix} p_i + p_r \\ p_i - p_r \end{bmatrix} \tag{9}$$

Rearranging Eqs. (8) & (9) solving for the transfer matrix M gives

$$\begin{bmatrix} M_{11} \\ M_{12} \end{bmatrix} = \begin{bmatrix} p_t & p_t \\ p_i + p_r & p_r - p_i \end{bmatrix}^{-1} \begin{bmatrix} p_i + p_r \\ p_t \end{bmatrix}$$

$$\begin{bmatrix} M_{11} \\ M_{12} \end{bmatrix} = \begin{bmatrix} p_t & p_t \\ p_i + p_r & p_r - p_i \end{bmatrix}^{-1} \begin{bmatrix} p_i - p_r \\ -p_t \end{bmatrix}$$

Therefore, the transfer matrix for a single compliant unit can be written as follows,

$$\boldsymbol{M} = \frac{1}{2p_i p_t} \begin{bmatrix} p_i^2 - p_r^2 + p_t^2 & (p_i + p_r)^2 - p_t^2 \\ (p_i - p_r)^2 - p_t^2 & p_i^2 - p_r^2 + p_t^2 \end{bmatrix}$$

Therefore, a liner composed of N compliant units and $N - 1$ intermediate rigid segments, the transfer matrix for this rigid segment is given by

$$\boldsymbol{M_{L_s}} = \begin{bmatrix} cosk_{eff}L_s & isink_{eff}L_s \\ sink_{eff}L_s & cosk_{eff}L_s \end{bmatrix}$$

The overall transfer matrix M relates the upstream and downstream state vectors, $\boldsymbol{M_{tot}} = \boldsymbol{M^1 M}_{\boldsymbol{s}}^{\boldsymbol{1,2}} \boldsymbol{M^2} \cdots \boldsymbol{M_s^{N-1,N} M^N}$. The details of the transfer matrix method can be found in the study [24]. The overall complex transmission coefficient $p_{t,\text{tot}}$ of the multi-unit liner is obtained by solving the transfer-matrix system,

$$\begin{bmatrix} p_i + p_r \\ p_i - p_r \end{bmatrix} = \begin{bmatrix} M_{11} & M_{12} \\ M_{21} & M_{22} \end{bmatrix} \begin{bmatrix} p_{ex} \\ p_{ex} Z_{ex}^{-1} \end{bmatrix} \tag{10}$$

where p_{ex} is the pressure at the exit of the duct. Solving Eq. 8 gives

$$p_i + p_r = (M_{11} + M_{12} Z_{ex}^{-1}) p_{ex} \tag{11}$$

$$p_i - p_r = (M_{21} + M_{22} Z_{ex}^{-1}) p_{ex} \tag{12}$$

By adding Eqs. (11) and (12)

$$\frac{2p_i}{p_{ex}} = M_{11} + M_{21} + (M_{12} + M_{22})Z_{ex}^{-1}$$

In the presence of anechoic termination at the duct end $Z_{ex} = 1$, therefore, the p_{ex} is equal to the total transmitted pressure $p_{t,tot}$. Therefore, the total transmission loss of the multi-unit compliant liner can be estimated as

$$TL_{tot} = -20*log_{10}\frac{|p_{(t,tot)}|}{p_i} = -20*log_{10}(\mathcal{T})$$

2.3. Genetic algorithm framework

A standard Genetic Algorithm (GA) is a heuristic search method inspired by Charles Darwin's principles of natural selection and genetics. It simulates the evolution of candidate solutions across generations through selection, crossover, and mutation. The fundamental concept was pioneered by John Holland, who sought to understand adaptation in nature and import those mechanisms into computer systems. Holland et al. [25] formalized the framework of selection, crossover, and mutation. Later, David E. Goldberg [26] popularized GA by applying it to real-world problems, including gas pipeline control and other engineering challenges.

A GA begins by generating an initial population of individuals, each called a chromosome. Each chromosome represents a potential solution to the problem and is typically encoded as a string of parameters. Every chromosome is evaluated by an objective function, which quantifies how good the solution is via a calculated fitness score. Next, selection determines which chromosomes pass their genes to the next generation, giving higher-quality solutions a better chance of reproducing. Common selection methods include roulette wheel selection, tournament selection, and elitism [27]. After selection, crossover combines two parent chromosomes (numeric arrays) to create one or more offspring, using techniques such as single-point or uniform crossover.

Then, mutation introduces random changes to prevent premature convergence on a local optimum. Mutation maintains genetic diversity and allows the algorithm to explore entirely new regions of the search space. Finally, the offspring population replaces the old population, and the cycle repeats. The algorithm terminates when convergence is achieved - for instance, when the population becomes so similar that no further improvement is observed. GAs have been found highly useful and widely applied in the field of acoustic metamaterials, where many combinations with GA-based structural optimization can be found. Owing to their derivative-free nature and strong exploration capability, GAs are well suited for optimizing acoustic metamaterial geometries, where the objective landscape is typically non-convex, frequency-dependent, and governed by multiple coupled resonances. For example, GAs have been successfully used in designing chiral honeycomb membrane metamaterials for broadband noise suppression [28], metamaterial lenses for enhanced focusing effects [29], and achieving sophisticated acoustic cloaking . In this study, a chromosome consists of the values of the geometric design parameters to be optimized; specifically, the panel tension $T_{p,j}$ and the cavity depth $D_{c,j}$. As a result, the chromosome length is twice the number of compliant units, since each unit contributes two parameters.

The minimum transmission coefficient $\mathcal{T}$ equivalently, the maximum transmission loss *TL* is sought over the frequency interval $[f_L, f_U]$, evaluated with a 1 Hz resolution. The optimal geometric parameter set for the compliant units is obtained as the argument that maximizes the objective function F_{obj}, defined as

$$F_{obj} = \sum_{f=f_L}^{f_U} \mathcal{T}(f).$$

Note that $\mathcal{T}$ and *TL* are related by

$$TL = -20log_{10}(\mathcal{T}).$$

The optimization ranges for the design parameters are [0.02, 0.08] m for the cavity depth and [5, 10] N/m for the panel tension.

The design variables are, for each unit $j = 1, \dots, N$:

Panel tension $T_{p,j}$ (controlling the fluid-loaded resonance of unit j).

Cavity depth $D_{c,j}$ (controlling the reactive stiffness and effective mass loading).

In this study, $N = 5$ is adopted, consistent with the configuration in earlier study [20]. The design vector is thus

$$=\{T_{p_1},\dots,T_{p_5},D_{c_1},\dots,D_{c_5}\}$$

2.4. Objective function and constraints

The primary performance metric for optimization is to broaden the transmission loss spectrum over the excitation frequency regime i.e., $0.0029 \leq f \leq 0.1$ (50 Hz to 1700 Hz) below the duct cut-off frequency $f_{cutt-off}$= 0.5.

The design is subject to the following constraints:

Geometric realizability:

consistent with material limits and manufacturable pre-tension levels.

$D_{c_j}^{min} \leq D_{c_j} \leq D_{c_j}^{max}$ consistent with available duct wall thickness and cavity fabrication constraints.

Gradient constraints, either tension or cavity depth, vary linearly along the flow direction:

Increasing gradient: $T_{p_1} < T_{p_2} < \cdots < T_{p_5}$ and $D_{c_1} < \cdots < D_{c_5}$.

Decreasing gradient: $T_{p_1} > \cdots > T_{p_5}$ and/or $D_{c_1} > \cdots > D_{c_5}$.

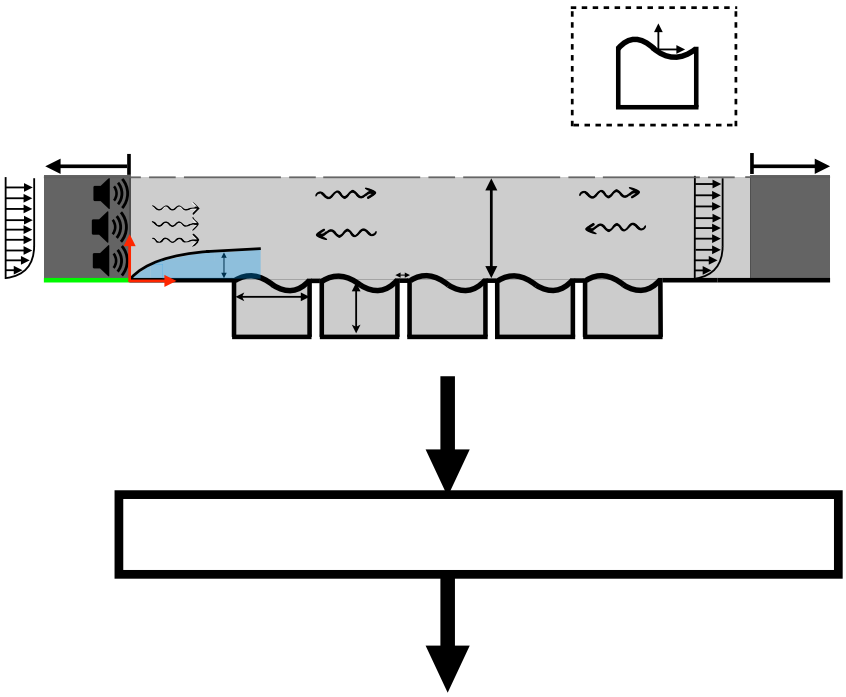

Figure 2.2: Problem schematics showing compliant duct and back-cavity and parametric optimization using GA.

These gradient constraints are motivated by findings of the study by Abdullah et al. [20] that demonstrated that increasing and decreasing resonance distributions (IRD/DRD) can widen the stopband and enhance *TL*.

2.5. GA cases considered

In the current study, we selected two optimization strategies (*OS* and *OS*) to investigate the ability of GA optimization to find the optimal design values for $T_{p,j}$ and $D_{c,j}$ for each compliant unit as shown in Fig 2.2.

i. *OS* : all $T_{p,j}$, $D_{c,j}$ are unconstrained, so no specific gradient constraints are defined; thus, the GA itself decides the values for each parameter for the compliant unit thus providing a combination of $T_{p,j}$, $D_{c,j}$ that provides a broadband *TL*.

ii. *OS* : In the gradient-constrained strategy the parameters $T_{p,j}$ and $D_{c,j}$ are required to follow a monotonic progression along the flow direction; however, whether an increasing or decreasing gradient is adopted is determined by the GA itself, driven solely by the broadband *TL* objective.

The baseline case with uniform resonance distribution will also be provided for better comparison. The *TL* spectra, along with transmission $\mathcal{T}$, reflection $\mathcal{R}$, and absorption $\mathcal{A}$ spectra, are compared to elucidate the impact of the distributed resonance surface compliance on the overall *TL* performance of the compliant liner.

3. Results and Discussions

3.1. Baseline URD liner: relation between and panel response

Figure 1 compares the transmission loss predicted by the analytical multi-unit model with the CESE–PEM simulation for the uniform-resonance multi-panel liner configuration. The analytical model reproduces the stopband between $f \approx 0.04$ and 0.07, including the two dominant *TL* peaks and the intervening troughs, with only moderate differences in peak magnitude relative to the CESE calculated *TL* spectra as shown in Fig. 3.1(a). The sufficient accuracy to capture the underlying dynamic behaviour of the compliant unit allows the analytical model to be used for the genetic optimization and parametric studies to achieve an efficient low-frequency broadband noise mitigation using that optimized flow liner. Figure 3.1b shows the *TL* of the baseline uniform-resonance-distribution (URD) liner together with the overall panel velocity V_{rms} as a function of frequency. The root mean square (RMS) quantity is defined as $V_{RMS} = \left(\sum_{j=1}^{N} V_j^2/2\right)^{1/2}$, where V_j is the complex velocity amplitude of unit mode j. A key observation, consistent with Huang's study, is that the major *TL* peaks and troughs do not coincide with local maxima or minima of V_{RMS}. Over the low- to mid-frequency range, V_{RMS} increases gradually as frequency rises, reflecting the increasing ease with which the incident plane wave excites the fundamental and higher modes of the compliant units, yet the *TL* curve exhibits alternating sharp peaks and dips superposed on this slow trend. In particular, strong *TL* peaks around the primary stopband coincide with frequencies where V_{rms} is elevated but not uniquely extreme, while several nearby frequencies with comparable or even higher V_{rms} yield only moderate *TL*. This lack of one-to-one correlation implies that the effectiveness of compliant liner in reflecting sound is not determined solely by the magnitude of the induced panel motion. This behaviour is attributed to the interference of sound radiated by different membrane modes, high TL occurs when the radiated field is

strongly out-of-phase with the duct plane wave in the downstream direction, so that destructive interference there suppresses transmission. In contrast, TL troughs occur when the modal contributions do not produce such an out-of-phase condition, thereby reducing the net reflection and allowing more energy to pass downstream.

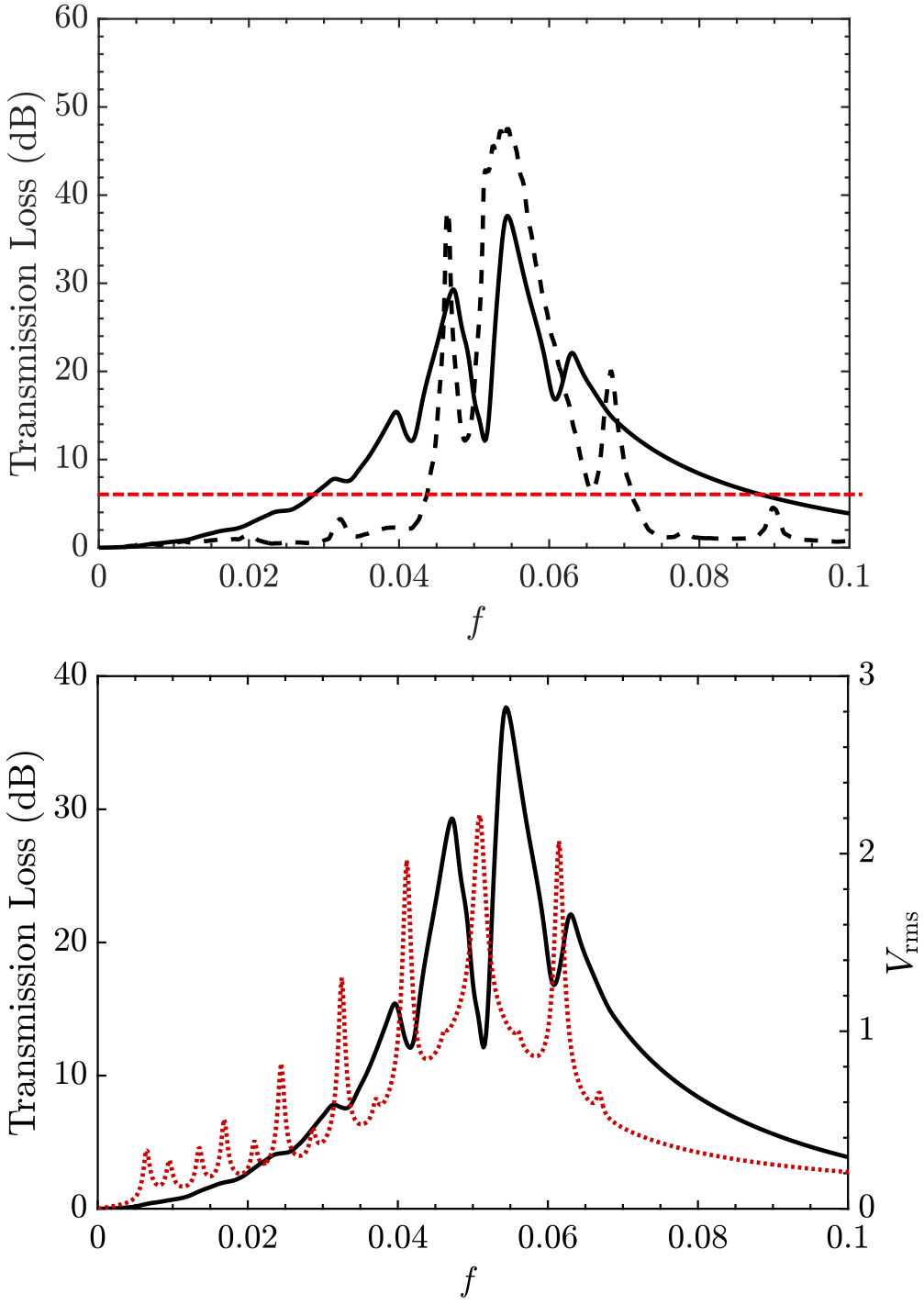

Figure 3.1: a) Comparison of TL spectra for multi-unit compliant system using analytical model and CESE-PEM calculation. b) Compliant system $_{RMS}$ vs. spectra comparison

The $\mathcal{A}$ -$\boldsymbol{V_{RMS}}$ plot in Fig. 3.2 shows that panel vibration is the primary mechanism associated with the absorption of the acoustic energy by the compliant system. The absorption coefficient is defined as $\mathcal{A} = 1 - \mathcal{T} - \mathcal{R}$, and the global panel velocity V_{rms} exhibits nearly coincident peaks, with the most pronounced maxima occurring near $f \approx 0.0325, 0.041, 0.051,$ and 0.061, and the largest peak at $f \approx 0.049$. This close correspondence indicates that whenever the compliant units respond strongly at their fluid-loaded resonant frequencies, a substantial portion of the incoming acoustic power is converted into structural vibration and dissipated, rather than being transmitted or purely reflected.

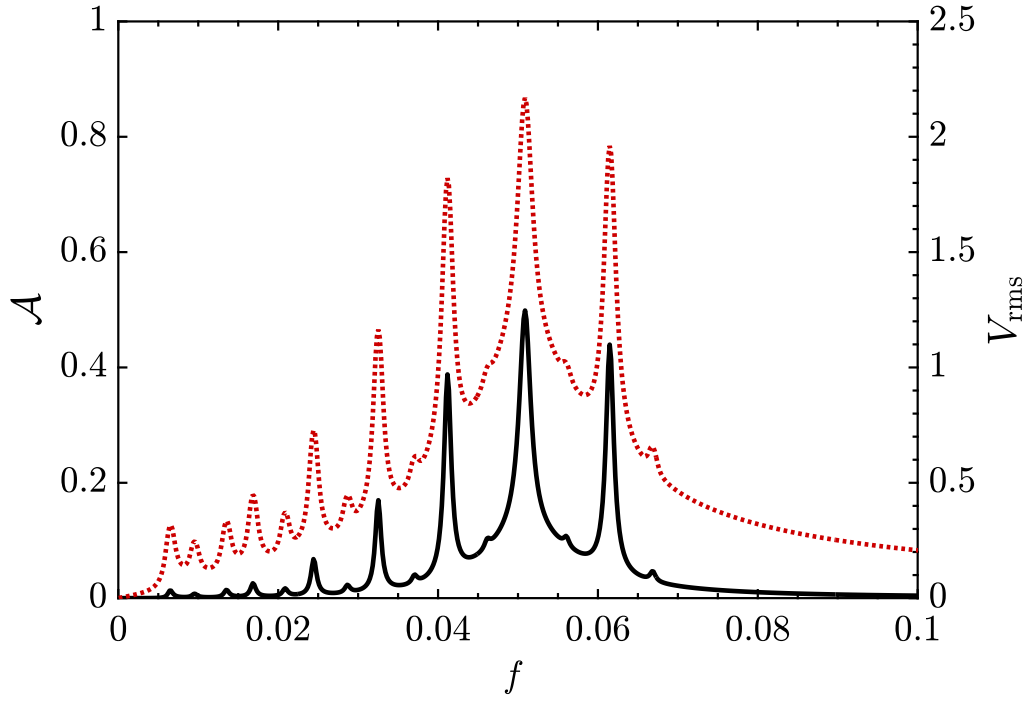

Figure 3.2:Comparison of the average absorption coefficient (—)and panel dynamics ()

This behaviour is consistent with findings in the numerical studies [18,20] that demonstrate that absorption in the compliant liner is a direct consequence of aeroacoustic–structural interaction. The associated vibrational energy is subsequently removed through structural damping and viscous losses in the surrounding fluid. Table 3.1 summarizes the normalized panel tension and cavity depth used in the uniform resonance distribution configuration.

Parametric configuration for uniform resonance distribution.

Parameters	CU	CU	CU	CU	CU
Panel Tension T_p	0.00180	0.00180	0.00180	0.00180	0.00180
Cavity Depth D_c	1.0	1.0	1.0	1.0	1.0

3.2. GA optimization

In the first stage, the compliant liner design space was explored using a non-gradient genetic algorithm, where all five compliant units were allowed to vary freely within the prescribed bounds of panel tension and cavity depth. The GA optimization was driven solely by the broadband transmission-loss objective, without enforcing any monotonic parametric gradient along the flow direction. The transmission loss provided by the random optimization in Fig. 3.3 shows a significantly higher number of resonant peaks clustered together, hence higher panel activity is generated. This higher activity of the compliant units and clustering of the resonant peaks produce overlapping stopbands, leading to a *TL* over a wider frequency spectrum. The *TL* bandwidth with a defined stopband criterion of 6.0 dB increases noticeably for the optimization case to $0.02 \leq f \leq 0.08$ as compared to $0.045 \leq f \leq 0.082$ for the uniform resonance distribution (URD) case with analytical prediction.

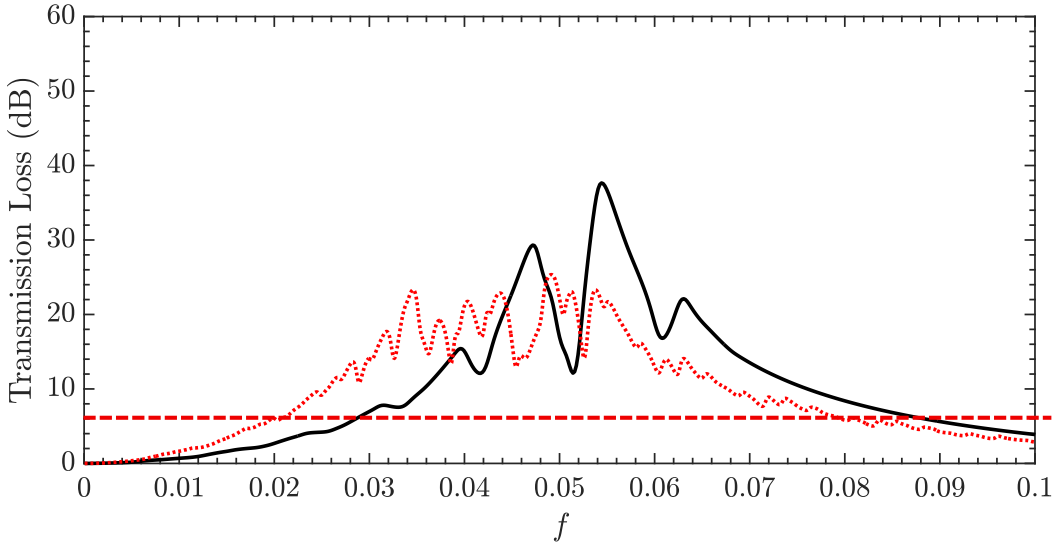

Figure 3.3: Comparison of *TL* spectra for uniform resonance distribution (URD) (—) and *OS* GA optimization (···) in a compliant system. 6.0 dB criterion (- - -)

It can also be observed that performance for the optimized case degrades slightly in the higher frequency in terms of peak *TL* magnitude but this reduction is compensated with higher and broader stopband in the desired low-frequency regime Therefore, the unconstrained GA solutions achieve substantial *TL* enhancement compared with the uniform-resonance baseline and stopband shifts to slightly lower frequencies, indicating that the GA successfully exploits combinations of units to push effective noise mitigation closer to the low-frequency regime. Figure 3.4 also presents the dynamical response of the compliant units for this optimized design. The V_{rms} traces of the five panels reveal intense panel activity, with many closely spaced resonant peaks that cluster in frequency, demonstrating that the liner resonates at a large number of frequencies and thereby produces overlapping unit stopbands and a more continuous high-*TL* region. In the very low-frequency range, i.e., $f \leq 0.02$, the panels already exhibit appreciable vibration, yet the transmission loss remains modest, which reinforces the conclusion drawn earlier that the magnitude of panel motion alone does not determine *TL*; the interference pattern between the scattered and incident fields, rather than absorption associated with large V_{rms}, is the primary factor governing transmission reduction.

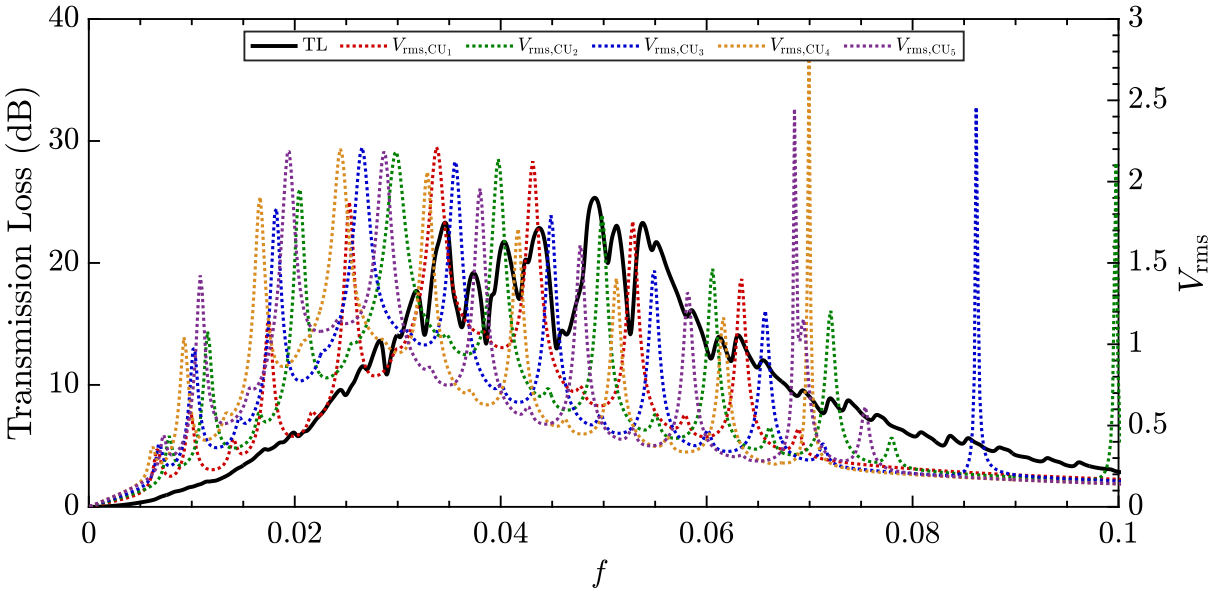

Figure 3.4: Comparison of total *TL* spectra of compliant system with panel activity contributed each of the compliant units, CU -CU for *OS* GA optimization.

To further elucidate the role of panel activity in the noise-mitigation process, Fig. 3.5 plots, for each compliant unit, the absorption coefficient $\mathcal{A}_{CU_j}$ together with the corresponding panel velocity $V_{rms_{CU_j}}$. The curves exhibit an almost one-to-one correspondence so that every prominent peak in $V_{rms_{CU_j}}$ is accompanied by a peak in $\mathcal{A}_{CU_j}$ as was already observed for the uniform-resonance distribution case. This confirms that, whenever a panel is strongly excited by the incident field, part of the acoustic energy extracted from the duct flow is converted into structural vibration and subsequently dissipated, so that panel vibration acts as an effective absorption mechanism in the optimized liner. Table 3.2 summarizes the optimized T_p and D_c values for the random GA optimization.

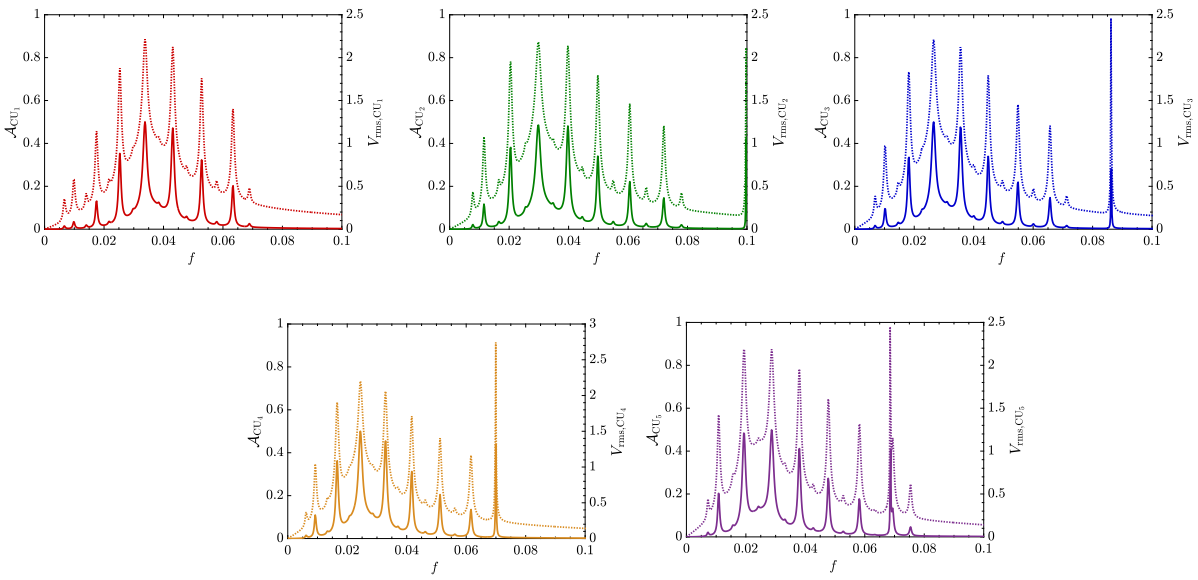

Figure 3.5: coefficient (—) vs. (⋯) comparison shows one-to-one correspondence for all five compliant units, i.e., CU - CU , for *OS* GA optimization.

Parametric configuration of compliant units with *OS* GA optimization.

Parameters	CU	CU	CU	CU	CU
Panel Tension T_p	0.0029	0.0030	0.0033	0.0028	0.0028
Cavity Depth D_c	2.0	1.5	4.0	3.0	1.0

3.3. GA Optimization

In the second stage, a gradient-distributed genetic algorithm is applied, in which the constraints are imposed to enforce a monotonic arithmetic progression of parameters along the liner. The panel tensions corresponding to fluid-loaded resonant frequencies of the five compliant units are allowed to either increase or decrease along the flow direction compared to their upstream neighbour, according to the chosen gradient direction. As a result, the GA explores those combinations that provide a monotonic gradient surface-resonance distribution, as shown in Table 3.3.The cavity depth D_c increases linearly downstream, whereas the panel tension T_p is chosen near the upper limit of the admissible range and remains almost identical for all compliant units, with CU being the only exception. Figure 3.6 shows that for the constrained GA optimization, the *TL* stopband is shifted to the higher frequency regime, i.e., $0.05 \leq f \leq 0.1$ as compared to the random GA optimization. The number of pronounced *TL* peaks within this stopband is also reduced, implying that the constraints imposed on the gradient of T_p and D_c limit the ability to cluster compliant unit resonances and to fully exploit multi-unit aeroacoustic-structural interaction. Figure 3.7 compares the total *TL* of the gradient-distributed liner with the combined rms response of all compliant units. The *TL* curve confirms that the main stopband of the gradient-constrained design is located in the higher-frequency range around $f \approx 0.06 - 0.08$, with peak attenuation levels comparable to those obtained previously but over a narrower band than in the freely distributed GA case.The superposed V_{rms} traces show that the compliant panels still exhibit strong vibratory activity, but the V_{rms} peaks are shifted towards the higher frequency region; therefore, *TL* remains moderate in the region $0.02 \leq f \leq 0.05$. It can also be observed that the V_{rms} peak overlapping between the panels is also reduced as compared to the random or free GA optimization case. This behaviour reinforces the conclusion that, under gradient constraints, the GA cannot cluster the unit resonances as effectively as in the random optimization, so the multi-unit interference

pattern is less favourable for generating a wide low-frequency stopband. The panels continue to extract energy from the acoustic field and the grazing flow, as indicated by the elevated V_{rms}, but only those frequencies at which their scattered fields combine coherently in reflection lead to high *TL*, while other frequencies with comparable panel motion yield only modest attenuation. Consequently, the gradient-distributed liner remains an effective broadband attenuator, but its performance is shifted toward higher frequencies and relies on fewer, more isolated resonance-assisted peaks than the freely distributed GA design.

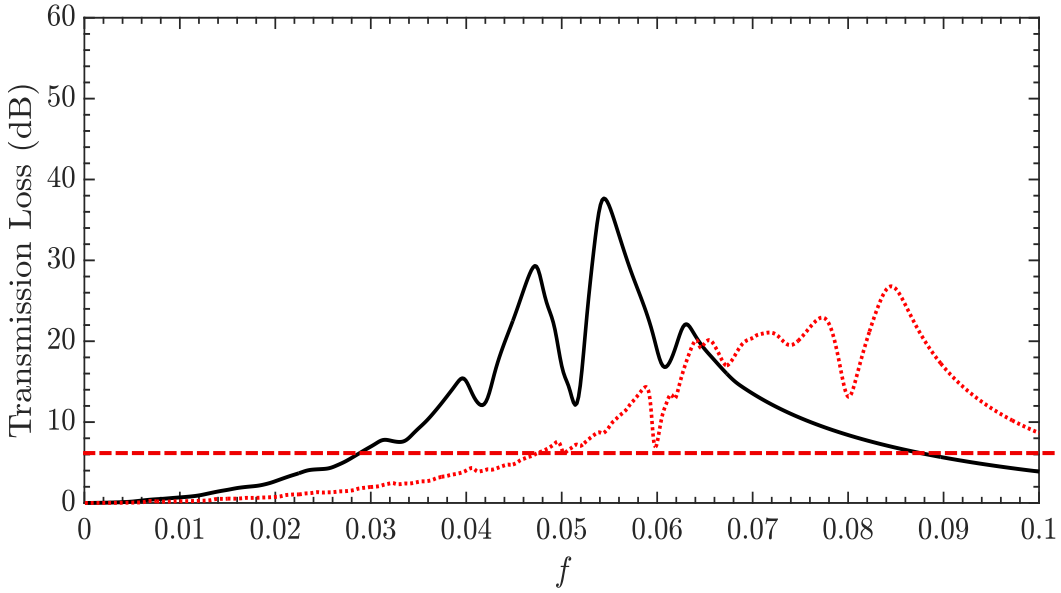

Figure 3.6: Comparison of *TL* spectra obtained using analytical model for uniform resonance distribution (URD) (—) and *OS* resonance distribution (···) in a compliant system. 6.0 dB criterion (- - -).

The absorption–velocity plots in Fig. 3.8 show that the relationship between panel motion and local dissipation remains intact. For each compliant unit, the absorption coefficient $A_{\mathrm{CU}\,j}$ and the corresponding rms velocity $V_{\mathrm{rms,CU}\,j}$ exhibit almost coincident peaks over the whole band, indicating that whenever a unit is strongly excited, it effectively extracts acoustic energy from the grazing-flow field and converts it into structural vibration and subsequent dissipation. This one-to-one correspondence is consistent with the behaviour observed for the uniform-resonance and freely distributed cases and confirms that, even under gradient constraints, panel vibration still underpins the absorption mechanism of each

compliant cell. A similar trend of the shifting of the resonance behaviour of the compliant unit towards the higher frequency region is also exhibited in the $A_{\mathrm{CU}j}$ vs. $V_{\mathrm{rms,CU}j}$ plots as compared to the previous case of random optimization.

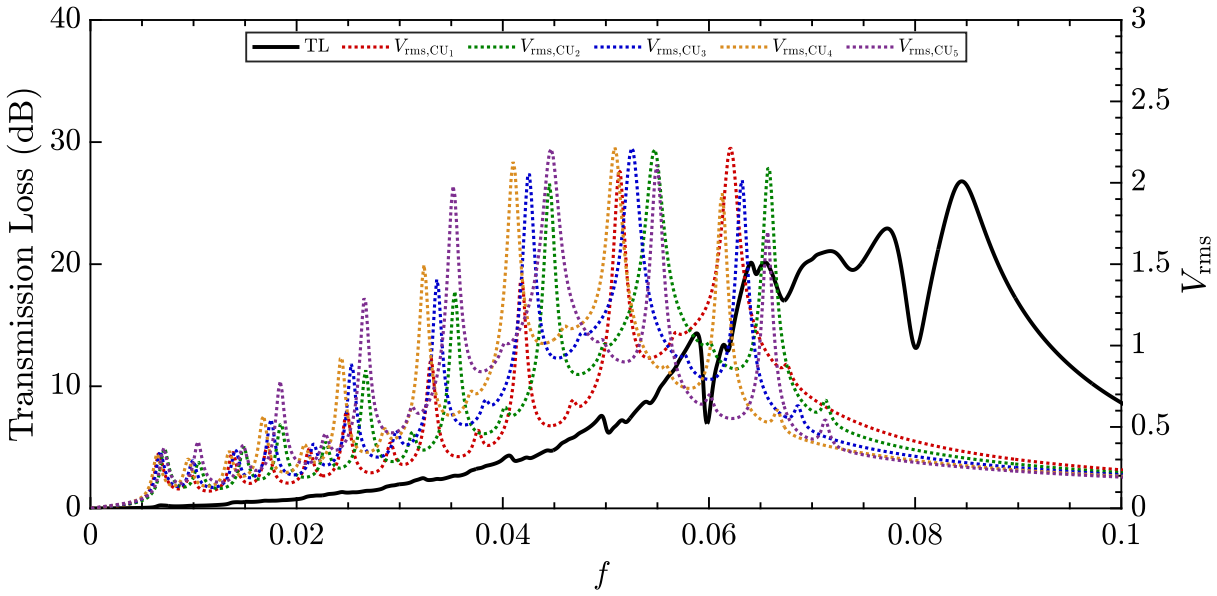

Figure 3.7: Comparison of total *TL* spectra of compliant system with panel activity contributed by each of the compliant units, CU -CU for *OS* GA optimization.

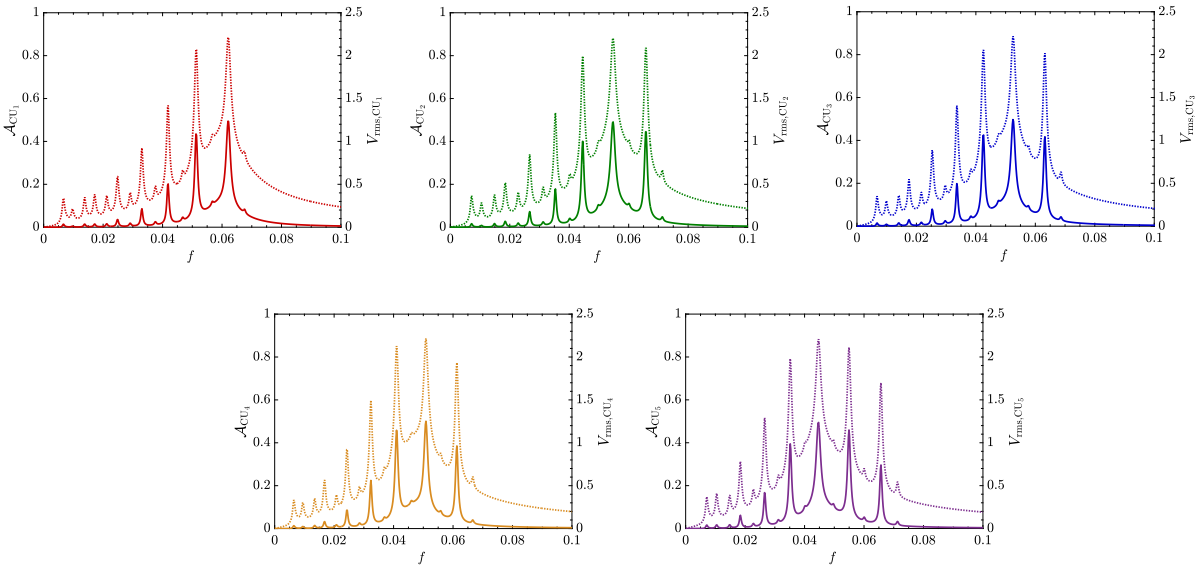

Figure 3.8: coefficient (—) vs. (⋯) comparison shows once to one correspondence for all five compliant units, i.e., CU - CU , *OS* GA optimization.

Therefore, we may deduce due to the shift of resonant $V_{\mathrm{rms,CU}j}$ towards the higher frequency region and reduced overlapping of resonant behaviour in the spectrum $0.02 \leq f \leq 0.05$, we see reduced *TL* performance in the low-frequency region for gradient constraint optimization.

Parametric configuration for *OS*			GA optimized GA distribution.		
Parameters	CU	CU	CU	CU	CU
Panel Tension T_p	0.00189	0.0035	0.0035	0.0034	0.0031
Cavity Depth D_c	0.6	0.8	1.0	1.20	1.40

4. Time Domain Aeroacoustic Analysis

The perturbation evolution method (PEM) is employed as a reduced-order, time-domain alternative to full direct aeroacoustic simulation (DAS). Arif et al. (2023) demonstrated that PEM retains the essential nonlinear flow–acoustic interactions with accuracy comparable to DAS, but its greatly reduced cost, i.e., only 10% of the computational resources are required as compared to DAS. In this work, PEM is applied, for the first time, to low-frequency broadband acoustics in duct flows. The steady base flow is obtained by time-averaging a DAS solution; while the Navier–Stokes equations are linearized about it to evolve small perturbations in time. A carefully chosen source term $\boldsymbol{S}$ keeps the base flow temporally steady in the absence of perturbations, so the resulting linear system governs the propagation of infinitesimal disturbances in a form that is mathematically equivalent to the homogeneous nonlinear equations.

$$\frac{\partial \boldsymbol{U}}{\partial t} + \frac{\partial \boldsymbol{F}}{\partial x} + \frac{\partial \boldsymbol{G}}{\partial y} = \boldsymbol{S}.$$

Considering as the small perturbation added to the base flow $\boldsymbol{U}_{\boldsymbol{base}}$ the instantaneous variable can be written as $= \boldsymbol{U}_{\boldsymbol{base}}$. Substituting the into Eq. (1) gives

$$\Rightarrow \frac{\partial(\boldsymbol{U_{base}} + \boldsymbol{U'})}{\partial t} + \left[\frac{\partial \boldsymbol{F}}{\partial x} + \frac{\partial \boldsymbol{G}}{\partial y}\right]' = 0,$$

where $\partial \boldsymbol{U_{base}} / \partial t = 0$ and $\boldsymbol{S}$ is chosen to be the spatial gradient of the base flow. The above equation reduces to a reduced-order model of the full nonlinear N-S equations, representing linear propagation of the infinitesimal disturbance as below:

$$\frac{\partial \boldsymbol{U'}}{\partial t} + \left[\frac{\partial \boldsymbol{F}}{\partial x} + \frac{\partial \boldsymbol{G}}{\partial y}\right]' = 0. \tag{13}$$

The perturbation model represented above is solved with normalized one-dimensional nonlinear Von Karman's plate equation representing the panel dynamics [30]. The CESE performs calculations in a strongly coupled manner; thus, the interactions among the flow field, acoustic field, and the structural dynamics of the elastic panels are simultaneously solved at each time step [20].

4.1. High-fidelity mechanism for the liner

Figure 4.1(a) compares the transmission loss spectra for three cases. It can be observed that the uniform-resonance configuration has limited transmission ($\mathcal{T}$) mitigation in a narrow *TL* stopband. In contrast, the analytically optimized random design exhibits a much broader low-frequency stopband, extending from roughly $f \approx 0.02$ to 0.066 with multiple overlapping peaks of order 20–25 dB, confirming that non-graded parameter distributions can substantially enhance broadband performance. The CESE–PEM *TL* for the random GA configuration closely follows the shape and level of the analytical prediction over the main stopband, with only modest smoothing of the sharpest features, demonstrating good consistency between the reduced-order multi-unit model and the fully coupled flow–acoustic–structure simulation. Importantly, the red curve remains significantly above the blue reference across most of the

low-frequency range, indicating that the optimized liner retains its superior broadband attenuation once all flow effects and nonlinear couplings are resolved numerically. This agreement both validates the analytical Huang-based transfer-matrix framework used in the GA and confirms that the randomly distributed multi-panel design offers a clear improvement over the uniform-resonance baseline in a realistic duct-flow environment.

Similarly, acoustic coefficients $\mathcal{T} - \mathcal{R} - \mathcal{A}$ shown in Fig. 4.1(b) provide further insights into the mechanism of noise mitigation provided by the compliant liner system. The absorption coefficient $\mathcal{A}$ is noticeably broadened, and the four (I-IV) absorption peaks are identified in Fig. 4.1(b), which can be attributed to the overlapping resonant responses of the elastic panels over a wide range of frequencies. This clustering of the overlapping resonant frequencies of the compliant panels has been identified earlier in the V_{rms} plot shown in Fig. 3.4. Therefore, increased absorption along with the intrinsic reflection supports the interpretation that the randomly GA-optimized liner configuration enhances aeroacoustic–structural interaction by distributing the surface compliance along the liner, thereby sustaining stronger absorption and improved broadband noise mitigation.

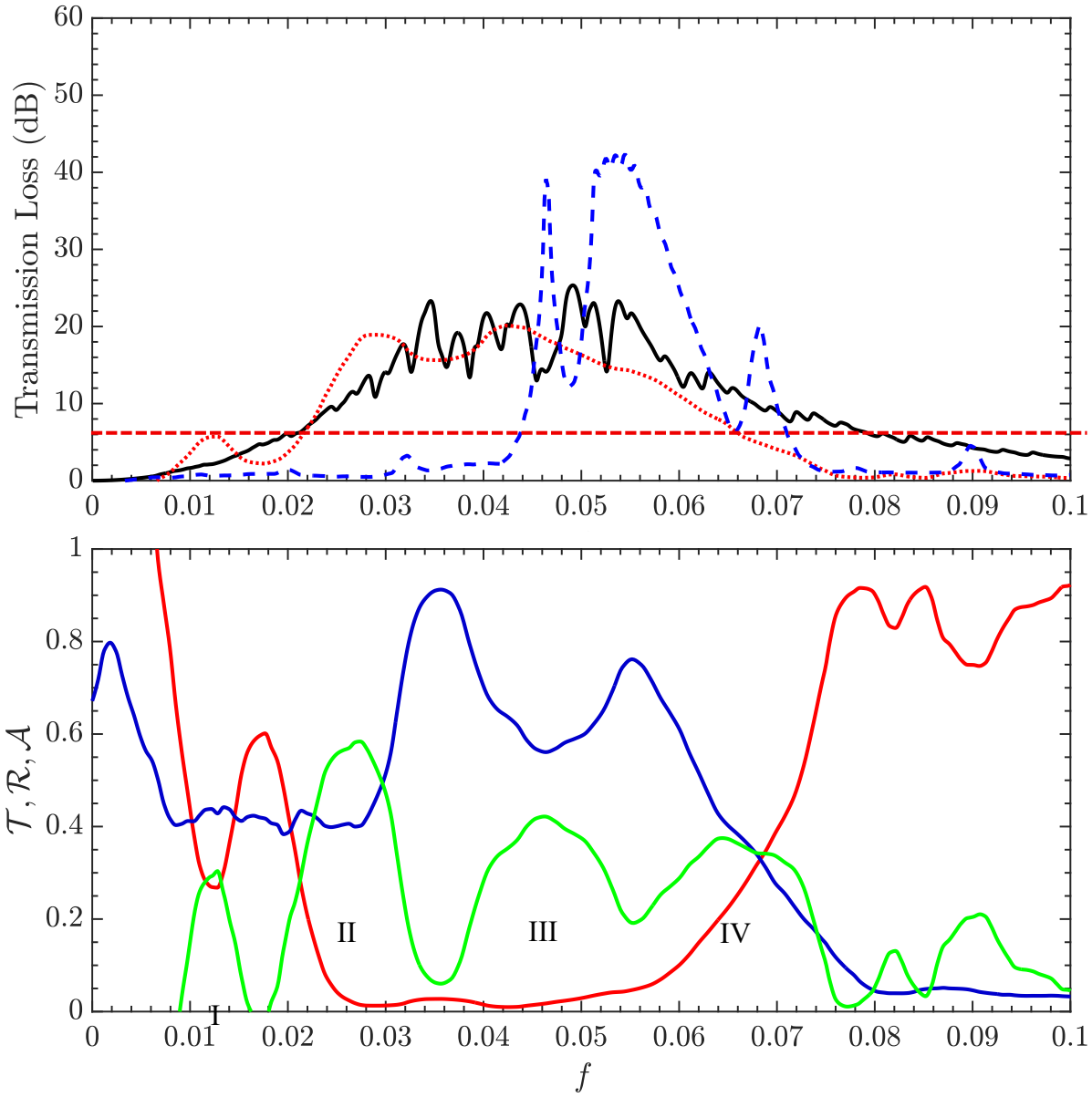

Figure 4.1: (a) Transmission loss spectra for three liner configurations: analytical OS GA-optimized (—), numerical OS (···), uniform resonance distribution (URD) (- - -) [20].

(b) Acoustic coefficients and trends showing the overall noise mitigation mechanism.

4.2. Panel Dynamics analysis for the liner

The broadening of *TL* spectrum identified in the *TL* spectra comparison and $\mathcal{T} - \mathcal{R} - \mathcal{A}$ coefficient analysis shown in Fig. 4.1(a) & (b) is further explained by the vibrational characteristics of the compliant panels in the liner system. The vibrational velocities $\dot{w}_p$ of all panels in the compliant system are shown in Fig. 4.2. It can be observed that in the low-frequency regime, the compliant panels show higher vibrational velocity, thus suggesting that

panels are effectively targeting these low frequencies. This further explains the widening of the absorption coefficient observed in the $\mathcal{T} - \mathcal{R} - \mathcal{A}$ plot shown in Fig. 4.1(a). The contour plot in Fig. 4.2 shows increased velocities across all the compliant panels, noticeably in the low-frequency regime. i.e., $0.01 \leq f \leq 0.04$. It can be see that each panel is responding to a distinct frequency, thus all the five panel combined provides increased panel vibration is observed for a range of frequency $0.01 \leq f \leq 0.04$, thus forming an overlapping region of heighted panel activity which was mechanism identified earlier in the V_{rms} plot from the analytical solution shown in Fig. 3.4. Therefore, this numerical result further validates the idea of the randomly optimized distributed resonance leverages the aeroacoustic-structural resonances to provide a broadband noise reduction. It should also be noted that the reflection $\mathcal{R}$ plays a significant in the overall $\mathcal{T}$ loss and overtake $\mathcal{A}$ for the higher frequency region.

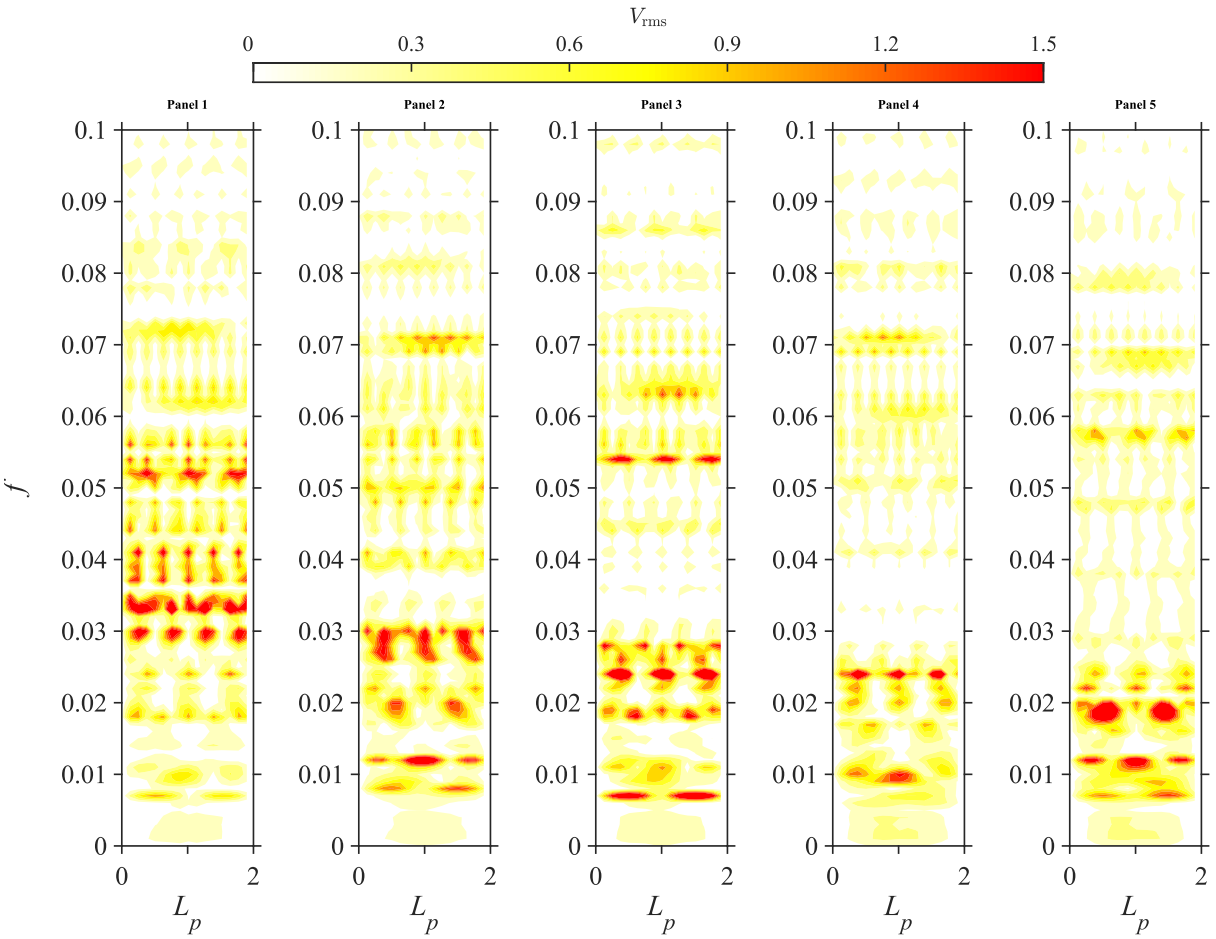

Figure 4.2: Panel dynamics showing the spectral distribution of vibrational velocity ( ) of all the compliant panel in the random GA optimized resonance distribution configuration.

In Fig. 4.3, the panel dynamics are directly compared with the enhanced absorption region identified in Fig. 4.1(b), clearly illustrating the overlap of the resonant peaks of the compliant panels. The first three compliant panel are the most active over a broad frequency range, with the first panel exhibiting the strongest response and acting as the dominant contributor to the system's overall noise-mitigation performance, while the farthest downstream panels (P and P) appear to target the lower frequency region . This finding is consistent with the earlier study [20] on compliant liners with gradient surface resonance compliance. It is also worth noting that, given the dominant response of the first panel, increasing the panel length of this upstream unit could further enhance its effective compliance and potentially yield additional transmission-loss improvement contributed by this panel.

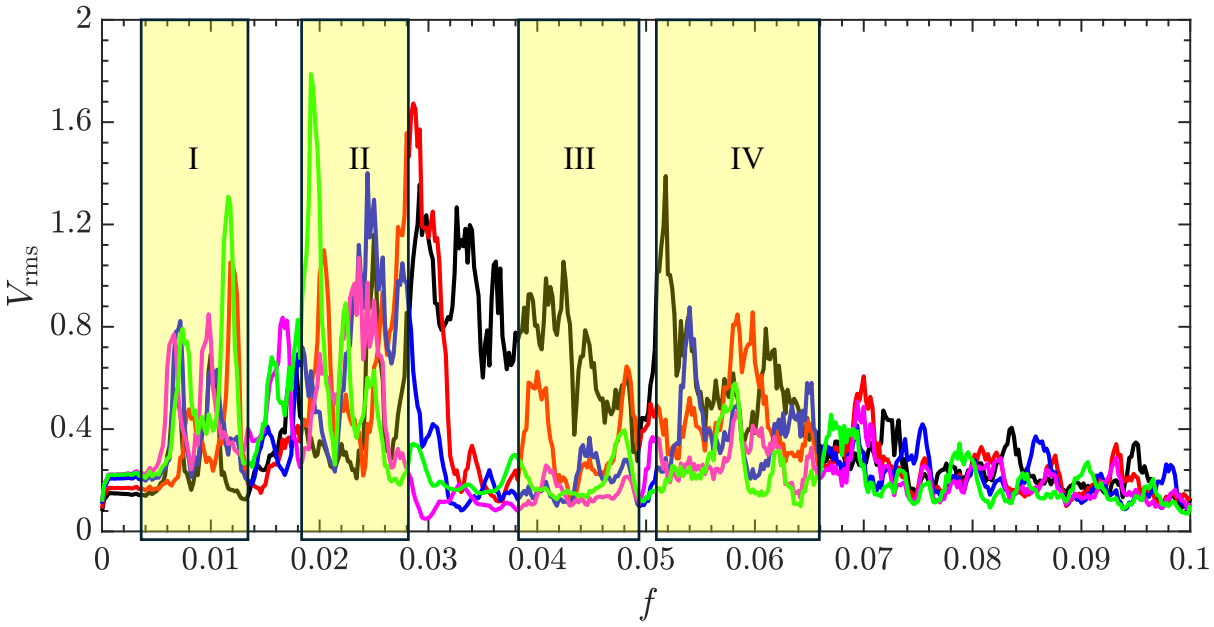

Figure 4.3: Panel dynamics showing the spectral distribution of vibrational velocity ( ) with highlighted increased regions (I-IV). P (), P ( ), P ( ), P ( ) and P ( )

5. Conclusions

The present study has examined broadband noise mitigation in a flow duct using multiple cavity-backed elastic panels, where the surface compliance is distributed by using genetic optimization based on a robust analytical model. In the study, two GA strategies were

considered, namely a freely distributed (random) parameterization and a gradient-constrained parametric distribution along the compliant. In order to validate the genetic optimization, high-fidelity time-domain CESE simulations were performed. The results demonstrate that, by appropriately distributing the fluid-loaded panel resonances using panel tension T_p and cavity depth D_c, stronger aeroacoustic–structural interactions can be exploited to achieve broadband transmission loss. The main findings and design implications are summarized below.

The transfer-matrix framework based on the analytical model accurately predicts the *TL* of multi-unit cavity-backed panel liners and agrees well with high-fidelity CESE–PEM simulations over the main stopband.

Freely distributed GA optimization (random GA) produces clustered fluid-loaded resonances, leading to overlapping unit stopbands, a wider low-frequency *TL* band, and a lower stopband onset than the URD and gradient-constrained designs, while maintaining comparable peak *TL*.

Gradient-distributed GA designs, in which cavity depth and panel tension follow a monotonic trend, remain effective but shift the stopband toward higher frequencies and reduce the number of strong *TL* peaks, because the constraints limit resonance clustering and weaken multi-unit interference.

Analysis of unit-wise V_{rms} and absorption shows an almost one-to-one correspondence between panel resonance and local absorption for all configurations, confirming that the panels extract energy from the flow and acoustic field, and that absorption is governed by aeroacoustic–structural interaction rather than by material losses alone.

The most upstream panels, particularly CU1, consistently exhibit the strongest vibratory response and contribute disproportionately to broadband attenuation, suggesting that selectively increasing the length or compliance of the first unit could further enhance the liner's low-frequency *TL*.

Acknowledgements

The authors gratefully acknowledge the support from the Research Grants Council of the Government of Hong Kong Special Administrative Region under Grant No. 15229924. The first author is grateful for the stipend support to his study tenable at the Department of Mechanical Engineering, The Hong Kong Polytechnic University.

6. References:

[1] Egaña, J. M., Díaz, J., and Viñolas, J., "Active Control of Low-Frequency Broadband Air-Conditioning Duct Noise," *Noise Control Engineering Journal*, Vol. 51, No. 5, 2003, pp. 292–299.

[2] Ibarra-Zarate, David I, Navas-Reascos, Gustavo, and Padilla-Ortiz, AL, "Passive Noise Control in Buildings: An Engineering Case Study of Ducted Systems," *Building Services Engineering Research & Technology*, Vol. 42, No. 6, 2021, pp. 751–762. https://doi.org/10.1177/01436244211019635

[3] Ouis, D., Hassanain, M. A., Alshibani, A., and Ghaithan, A. M., "Noise from Heating, Ventilation, and Air Conditioning (HVAC) Systems: A Review of Its Characteristics, Effects and Control," *Journal of Building Engineering*, Vol. 112, 2025, p. 113770. https://doi.org/https://doi.org/10.1016/j.jobe.2025.113770

[4] Zhang, X., Yang, C., Cheng, L., and Zhang, P., "An Experimental Investigation on the Acoustic Properties of Micro-Perforated Panels in a Grazing Flow," *Applied Acoustics*, Vol. 159, 2020, p. 107119.

[5] Li, Y., and Choy, Y. S., "Broadband and Low-Frequency Sound Absorption of Compact Meta-Liner under Grazing Flow," *Applied Acoustics*, Vol. 224, 2024, p. 110146. https://doi.org/https://doi.org/10.1016/j.apacoust.2024.110146

[6] Lee, Y. Y., Lee, E. W. M., and Ng, C. F., "Sound Absorption of a Finite Flexible Micro-Perforated Panel Backed by an Air Cavity," *Journal of Sound and Vibration*, Vol. 287, No. 1, 2005, pp. 227–243. https://doi.org/10.1016/j.jsv.2004.11.024

[7] Langfeldt, F., and Gleine, W., "Membrane- and Plate-Type Acoustic Metamaterials with Elastic Unit Cell Edges," *Journal of Sound and Vibration*, Vol. 453, 2019, pp. 65–86. https://doi.org/10.1016/j.jsv.2019.04.018

[8] Landau, I. D., Meléndez, R., Dugard, L., and Buche, G., "Robust and Adaptive Feedback Noise Attenuation in Ducts," *IEEE Transactions on Control Systems Technology*, Vol. 27, No. 2, 2019, pp. 872–879. https://doi.org/10.1109/TCST.2017.2779111

[9] Song, Xiang, Xu, Jingjian, Yuan, Tianyue, Sun, Wenhao, Sui, Dan, Xiao, Heye, and Zhou, Jie, "An Investigation on the Modelling of a Finite Porous Liner for the Sound Propagation in a Rectangular Duct," *Journal of Vibration and Control*, Vol. 30, Nos. 1–2, 2024, pp. 406–417. https://doi.org/10.1177/10775463221147734

[10] Chan, C., Perrey-Debain, E., Ville, J.-M., and Poirier, B., "Numerical Determination of Transmission Losses of a Turbofan Inlet Duct Lined with Porous Materials," *Applied Acoustics*, Vol. 117, 2017, pp. 86–93. https://doi.org/https://doi.org/10.1016/j.apacoust.2016.09.024

[11] Wu, G., Guan, Y. H., Ji, C., and Gay, F. Y. X., "Experimental Studies on Sound Absorption Coefficients of Perforated Pipes with Bias-Grazing Flows at Low Mach and Strouhal Number," *Aerospace Science and Technology*, Vol. 107, 2020, p. 106255. https://doi.org/https://doi.org/10.1016/j.ast.2020.106255

[12] Zhao, D., Ji, C., and Yin, M., "Experimental Investigation of Geometric Shape Effect of Coupled Helmholtz Resonators on Aeroacoustics Damping Performances in Presence of Low Grazing Flow," *Aerospace Science and Technology*, Vol. 128, 2022, p. 107799. https://doi.org/https://doi.org/10.1016/j.ast.2022.107799

[13] Zhang, X., and Cheng, L., "Acoustic Silencing in a Flow Duct with Micro-Perforated Panel Liners," *Applied Acoustics*, Vol. 167, 2020, p. 107382. https://doi.org/https://doi.org/10.1016/j.apacoust.2020.107382

[14] Huang, L., "A Theoretical Study of Duct Noise Control by Flexible Panels," *The Journal of the Acoustical Society of America*, Vol. 106, No. 4, 1999, pp. 1801–1809. https://doi.org/10.1121/1.427930

[15] Huang, L., “Modal Analysis of a Drumlike Silencer,” *The Journal of the Acoustical Society of America*, Vol. 112, No. 5, 2002, pp. 2014–2025. https://doi.org/10.1121/1.1508778

[16] Huang, L., “Parametric Study of a Drum-like Silencer,” *Journal of Sound and Vibration*, Vol. 269, No. 3, 2004, pp. 467–488. https://doi.org/10.1016/S0022-460X(02)01642-5

[17] Choy, Y. S., and Huang, L., “Effect of Flow on the Drumlike Silencer,” *The Journal of the Acoustical Society of America*, Vol. 118, No. 5, 2005, pp. 3077–3085. https://doi.org/10.1121/1.2047207

[18] Fan, H. K. H., Lam, G. C. Y., and Leung, R. C. K., “Spatio-Temporal Aeroacoustic–Structural Responses of Cavity-Backed Elastic Panel Liner Exposed to Grazing Duct Flow,” *Journal of Fluids and Structures*, Vol. 102, 2021, p. 103228. https://doi.org/10.1016/j.jfluidstructs.2021.103228

[19] Lam, G. C. Y., Leung, R. C. K., Fan, H. K. H., and Aurégan, Y., “Effect of Back Cavity Configuration on Performance of Elastic Panel Acoustic Liner with Grazing Flow,” *Journal of Sound and Vibration*, Vol. 492, 2021, p. 115847. https://doi.org/10.1016/j.jsv.2020.115847

[20] Abdullah, A., Leung, R. C. K., Lam, R. K. H., Naseer, M. R., and Arif, I., “Mitigation of Broadband Duct Flow Noise Using Liner with Gradient Surface Resonant Compliance,” *Journal of Fluids and Structures*, Vol. 140, 2026, p. 104452. https://doi.org/https://doi.org/10.1016/j.jfluidstructs.2025.104452

[21] Lam, W. K., Krynkin, A., Umnova, O., and Tang, S. K., “Simultaneous Acoustic Perfect Absorption and Rainbow Trapping via Topologically Optimized Sub-Wavelength Multi-Slit Sonic Crystal Metamaterials,” *npj Acoustics*, Vol. 2, No. 1, 2026, p. 2. https://doi.org/10.1038/s44384-025-00026-5

[22] Choi, S., and Kim, Y.-H., "Sound-Wave Propagation in a Membrane–Duct (L)," *The Journal of the Acoustical Society of America*, Vol. 112, No. 5, 2002, pp. 1749–1752. https://doi.org/10.1121/1.1509761

[23] Doak, P. E., "Fundamentals of Aerodynamic Sound Theory and Flow Duct Acoustics," *Journal of Sound and Vibration*, Vol. 28, No. 3, 1973, pp. 527–561. https://doi.org/10.1016/S0022-460X(73)80039-2

[24] Choy, Y. S., and Huang, L., "Multiple Drumlike Silencer for Low Frequency Duct Noise Reflection," *Applied Acoustics*, Vol. 70, No. 11, 2009, pp. 1422–1430. https://doi.org/https://doi.org/10.1016/j.apacoust.2009.03.010

[25] Holland, J. H., "Adaptation in Natural and Artificial Systems: An Introductory Analysis with Applications to Biology, Control, and Artificial Intelligence," 1992.

[26] Goldberg, D. E., "Genetic Algorithms in Search, Optimization, and Machine Learning," Addison-Wesley, 1989.

[27] Sivanandam, S. N., and Deepa, S. N., "Genetic Algorithms," *Introduction to Genetic Algorithms*, edited by S. N. Sivanandam and S. N. Deepa, Springer Berlin Heidelberg, Berlin, Heidelberg, 2008, pp. 15–37. https://doi.org/10.1007/978-3-540-73190-0_2

[28] Li, D., Zigoneanu, L., Popa, B.-I., and Cummer, S. A., "Design of an Acoustic Metamaterial Lens Using Genetic Algorithms," *The Journal of the Acoustical Society of America*, Vol. 132, No. 4, 2012, pp. 2823–2833. https://doi.org/10.1121/1.4744942

[29] Pomot, L., Payan, C., Remillieux, M., and Guenneau, S., "Acoustic Cloaking: Geometric Transform, Homogenization and a Genetic Algorithm," *Wave Motion*, Vol. 92, 2020, p. 102413. https://doi.org/https://doi.org/10.1016/j.wavemoti.2019.102413

[30] Fan, H. K. H., Leung, R. C. K., and Lam, G. C. Y., "Numerical Analysis of Aeroacoustic-Structural Interaction of a Flexible Panel in Uniform Duct Flow," *The*

Journal of the Acoustical Society of America, Vol. 137, No. 6, 2015, pp. 3115–3126. https://doi.org/10.1121/1.4921285